Journal of Alloys and Compounds 962 (2023) 171086

Contents lists available at ScienceDirect

Journal of Alloys and Compounds

journal homepage: www.elsevier.com/locate/jalcom

Fatigue behavior of low-temperature hot isostatic pressed electron beam powder bed fusion manufactured Ti-6Al-4 V

K. Pandian [a,*], M. Neikter [a], F. Bahbou [b], A. Ganvir [c,d], T. Hansson [a,c], R. Pederson [a]

[a] University West, Department of Engineering Science, SE-461 86 Trollhättan, Sweden
[b] GE Additive, SE-435 33 Mölnlycke, Sweden
[c] GKN Aerospace Engine Systems, SE-461 38 Trollhättan, Sweden
[d] University of Turku, FI-20014 Turun yliopisto, Finland

ARTICLE INFO

Keywords:
Additive manufacturing
Electron beam melting
Hot isostatic pressing
Low cycle fatigue
Fatigue crack growth
Ti-6Al-4 V

ABSTRACT

Ti-6Al-4 V finds application in the fan and compressor modules of gas turbine engines due to its high specific strength. Ti-6Al-4 V components manufactured using one of the additive manufacturing (AM) techniques, the electron beam powder bed fusion (PBF-EB) process, has been an active area of research in the past decade. The fatigue life of such PBF-EB built Ti-6Al-4 V components is improved by hot isostatic pressing (HIP) treatment typically performed at about 920 ℃. The HIP treatment at 920 ℃ results in coarsening of α laths and reduced static strength and therefore a low-temperature HIP treatment is performed at about 800 ℃ to limit the impact on static mechanical properties. In the present work, the low cycle fatigue and fatigue crack growth behavior of such a modified HIP (low-temperature HIP) treated material is assessed and compared with the respective data for the standard HIP-treated material. The modified HIP-treated material has fatigue performance comparable to the standard HIP-treated material. This work suggests that the modified HIP treatment improves the static mechanical properties without significantly impacting the fatigue performance. Also, fatigue life predictions were made from the measured defect size at the crack initiation site using a linear elastic fracture mechanics tool. The life predictions show good agreement with the experimental values for defects greater than the intrinsic crack length, where life is well predicted by large-crack growth methodology.

1. Introduction

Ti-6Al-4 V is the most popular α + β titanium alloy used in aerospace engine applications due to its high strength to weight ratio and excellent mechanical properties [1,2]. In the last few decades, there has been an increased focus within the aerospace industry to use additive manufacturing (AM) to build Ti-6Al-4 V components [3–5]. The industry sees potential benefits with AM over traditional manufacturing such as reduced material wastage, reduced failure risk with a minimum number of parts and unique metallurgy producing comparable properties to conventional material [6,7]. Several AM techniques exist today and the microstructure and mechanical properties of Ti-6Al-4 V differ with the different techniques [8]. The AM-built Ti-6Al-4 V components have comparable yield strength, tensile strength and elongation properties to wrought material [9–12]. The high cycle fatigue life of the as-built material is significantly lower than wrought Ti-6Al-4 V and has a large scatter in fatigue life [13,14]. In contrast, the post-heat-treated (such as HIP-treated) AM-built material have shown a potential for equivalent or better fatigue performance compared to wrought material [15].

Electron beam powder bed fusion (PBF-EB) is one of the powder bed fusion techniques widely used for producing Ti-6Al-4 V alloy due to its high productivity and minimal residual stress compared to laser powder bed fusion [16]. PBF-EB built Ti-6Al-4 V has a lamellar microstructure comprised of α laths distributed within the columnar prior β grains [11,17–20]. The α lath morphology is highly dependent on the cooling rate and affects the alloy's fatigue properties. The β → α phase transformation in Ti-6Al-4 V begins at about 995 ℃ known as the β transus temperature [2]. For slower cooling rates, the α phase first nucleates along the β grain called grain boundary α laths (GB- α) that has a detrimental effect on fatigue properties [2,21]. As the transformation continues, either group of α laths grows from the prior β grain boundary into the grain as a "colony α" structure or α laths nucleate directly from the previously formed α laths within the prior β grains and grow into intertwined basketweave morphology.

* Corresponding author.
E-mail address: karthikeyan.thalavai-pandian@hv.se (K. Pandian).

https://doi.org/10.1016/j.jallcom.2023.171086
Received 15 December 2022; Received in revised form 1 June 2023; Accepted 20 June 2023
Available online 20 June 2023
0925-8388/© 2023 The Authors. Published by Elsevier B.V. This is an open access article under the CC BY license (http://creativecommons.org/licenses/by/4.0/).

The critical factor in increasing fatigue crack nucleation resistance in the microstructure is maximum dislocation slip length [2]. Crack initiation and stage I crack growth are hindered when the mean free slip paths are smaller, resulting in increased fatigue strength [22]. Compared to the basketweave microstructure, the lamellar microstructure with aligned α laths (colony α) has the longest crystallographic slip bands with planar slip extending across the colonies [23]. So, from the aspect of crack initiation, the fatigue performance would be better when there is a more significant fraction of basketweave morphology. Among materials with basketweave microstructure, the thickness of α laths determines the effective slip length [24]. So, a fine basketweave microstructure should have higher resistance to crack initiation than a coarser microstructure. On the other hand, as the crack propagates to several magnitudes of the microstructural feature, crack deflection and bifurcation become prominent for crack growth resistance [25]. A coarser lamellar structure provides more resistance to crack propagation than a finer structure due to a longer unfavorable crack propagation path after deflection [26]. So, in terms of crack propagation, coarser α laths or colonies may be beneficial for improved fatigue performance.

Defects present in as-built material that get exposed after machining mostly act as primary crack initiation sites rather than microstructural features [13]. The primary internal defects seen in the PBF-EB built Ti-6Al-4 V are porosity and lack of fusion (LoF) defects. Significant LoF defects in the material are primarily caused by poor process control [27]. Entrapped gases generally cause spherical pores, and for a process that operates in high vacuum conditions, the source of such defects would be the feedstock [28]. Following a post-processing procedure such as HIP treatment helps to reduce these internal defects and achieve an improved fatigue performance [29]. HIP treatment is typically performed at 920 ℃ with 100 MPa pressure, which coarsens the α laths and reduces the static strength of the material [9,17,30]. In an earlier study, considering a low temperature of 800 ℃ and increased pressure of 200 MPa for HIP treatment resulted in limited coarsening of α laths with less negative impact on the yield strength compared to the standard HIP process [31]. The effect of such a low-temperature HIP on the fatigue performance of PBF-EB built Ti-6Al-4 V is yet to be investigated.

In the present study, the low cycle fatigue (LCF) and fatigue crack growth (FCG) performance of a low-temperature HIP-treated material is investigated and compared with the corresponding properties of standard HIP-treated material. Even though the low-temperature HIP has improved the static mechanical properties, it is critical to understand the fatigue performance of such a HIP-treated material.

2. Materials and method

2.1. Materials and HIP treatment

Standard plasma atomized Ti-6Al-4 V powder from AP&C (Canada) with a nominal size distribution of 45–105 μm and d_{50} value of 69 μm was recycled to manufacture the experimental specimens. ARCAM Q20 plus PBF-EB machine running a standard 5.3.76 process theme with 50 μm layer thickness was used for the build. The powder chemical composition as measured by inductively coupled plasma optical emission spectroscopy (ICP-OES analysis) is reported in Table 1. The LCF specimens were built to a dimension of Ø15 mm× 105 mm long oriented vertically in the build chamber and later machined to Metcut drawing MRI 1027 (as per ASTM E606 requirements) after HIP treatment, as shown in Fig. 1. The HIP treatments were carried out in a Quintus QIH 21 M URC equipment at Västerås, Sweden. A standard HIP treatment was performed at 920 ℃, 100 MPa, 2 h hold time followed by uniform rapid cooling (URC) [31]. The modified HIP treatment was performed at 800 ℃, 200 MPa, 2 h hold time followed by URC [31]. 15 × 15 x 15 mm cubes were manufactured during the same build for metallographic investigations.

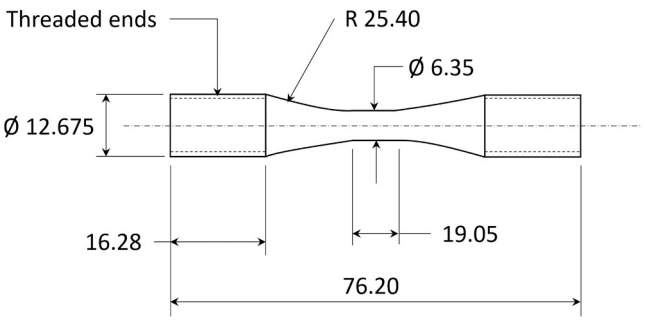

Fig. 1. LCF test specimen geometry. All dimensions are in mm. Drawing not to scale.

2.2. Metallographic investigation

Preparation of specimens for the metallographic study was done using conventional lab instruments. Images for the porosity analysis were taken in a light optical microscope (LOM) Zeiss AL10. The images were obtained from polished cross-sections. For microstructural investigations, the specimens were etched by immersing them in Barker's reagent for titanium (84 ml H_2O + 16 ml 50% HBF_4) for about 10–12 s and imaged using the same LOM. Initial analysis of the fracture surfaces was done in an Olympus SZX9 stereomicroscope. To perform further detailed fractography, a scanning electron microscope (SEM) ZEISS GeminiSEM 450 was used to obtain images at higher magnifications. The image analysis for porosity and α lath thickness measurement was done in ImageJ 1.52a [32]. For α lath thickness measurement, images were taken by LOM at 1000x magnification from the top, bottom, left, right, and center of the cross-sections prepared parallel and perpendicular to build directions (BD). Ridley [33] proposed a method to measure the interlamellar spacing which is used in this study to measure the α lath thickness. Straight lines of fixed length were drawn intersecting the α laths at different angles on the high magnification LOM images. Later, the intercepts were counted, and the total line length was divided by the intercept count to obtain the mean intercept spacing. Finally, a stereology correction factor 0.5 is applied to calculate the actual α lath thickness.

To investigate the average porosity distribution multiple images (about 33 images) were taken at 100x magnification using LOM and stitched together forming a total area of about 3 × 8 mm. The same procedure was repeated at three different locations in each cross-section to obtain maximum area coverage. The density measurement was also done using the Archimedes method as per ASTM B311–17 by using 15 × 15 x 15 mm cubes and distilled water as the liquid medium. Before measurement, all specimens were cleaned in an ultrasonic bath to remove any loose powder particles and impurities from the surface. Each specimen was measured three times to determine the average density of the specimen. The relative density of the specimen was then determined by comparing the measured density with the nominal density of Ti-6Al-4 V.

Table 1
Chemical composition of the plasma atomized Ti-6Al-4 V powder used in the PBF-EB process compared with ASTM F3001 requirements.

Element	Al	V	Fe	C	H	N	O	Ti
As-delivered (%)	6.350	3.920	0.200	0.010	0.002	0.010	0.127	Rem.
ASTM F3001 (%)	5.500– 6.500	3.500 – 4.500	< 0.250	< 0.080	< 0.012	< 0.050	< 0.130	Rem.

2.3. Fatigue testing

The two different groups of HIP-treated specimens were subjected to a fully reversed (R = −1) strain-controlled fatigue test performed at room temperature as per ASTM E606/E606M in a servo-hydraulic device Instron 8802. Six specimens were tested at a strain range of 0.9%, and four specimens were tested at 1.2% strain range for both modified HIP-treated (MH) and standard HIP-treated (SH) materials. The tests were conducted in strain control at a frequency of 0.5 Hz until 43,200 cycles. If the plastic strain was found to be less than 0.01%, then the test was switched to load control at a frequency of 10 Hz until failure or run out. The failure criteria were set to a 20% drop in peak load.

2.4. Low cycle fatigue properties

The number of cycles to failure is related to the strain-life by using the Basquin Coffin-Manson type relationship as shown in Eq. 1.

$$\Delta\varepsilon = \Delta\varepsilon_e + \Delta\varepsilon_p \tag{1}$$

$$\Delta\varepsilon_e = A(N_f)^{\alpha} \tag{2}$$

$$\Delta\varepsilon_p = B(N_f)^{\beta} \tag{3}$$

Where $\Delta\varepsilon$ - total strain range, $\Delta\varepsilon_e$ – elastic strain range, $\Delta\varepsilon_p$ - plastic strain range N_f – number of cycles to failure and A, B, α, β are material constants. The elastic strain range in Eq. 2 calculated from stress range at mid-life and modulus of elasticity using Hooke's law. The plastic strain range in Eq. 3 is the difference between the applied total strain range and calculated elastic strain range.

For strain ranges having an plastic component, the stress-strain response during loading and unloading do not overlap due to plastic deformation and result in hysteresis loops. The width of each hysteresis loop represents the plastic strain in the material during each cycle.

2.5. Fatigue crack growth

Fatigue crack growth tests were performed on the modified and standard HIP-treated specimens in air and R = −1 at Metcut Research Inc., Cincinnati, OH, USA. The details about Kb bar geometry and FCG test procedure are available in a previously published work [18]. Direct current potential drop was utilized to investigate the crack growth. The measured potential drop values were translated into crack sizes using the calibration curves developed at University West. The maximum stress intensity factor (SIF) values were obtained from NASGRO v10.00 using crack case SC30, "semi-elliptical surface crack in plate" [34]. The SIF range ΔK was calculated from the maximum SIF values (K_{max}) and strain ratio (R) using the Eq. 4.

$$\Delta K = K_{max}(1 - R) \tag{4}$$

The fatigue life predictions were performed using the SC30 crack description in NASGRO and the measurements from the defect that initiated the failure. The da/dN versus ΔK values for the standard and modified HIP-treated material obtained from the FCG test were used as the input data for material description in the software. The maximum and minimum stress at mid-life from the fatigue test was used as input loads to predict the fatigue life for each measured defect size.

3. Results

3.1. Microstructure

Fig. 2 shows the microstructure of the modified HIP-treated (Fig. 2a & c) and standard HIP-treated (Fig. 2b & d) materials parallel to the BD at two different magnifications. The white markings drawn in the low magnifications Fig. 2a & b depict the prior β grain boundaries. The prior β grains have a columnar morphology and grow epitaxially over several build layers. The prior β grains are similar in size for both HIP-treated conditions. The black markings in the high magnification Fig. 2c & d represent α laths. From the high magnification SEM images for modified HIP-treated (Fig. 2c) and standard HIP-treated (Fig. 2d) material, it appears the α laths are coarser in the standard HIP-treated material.

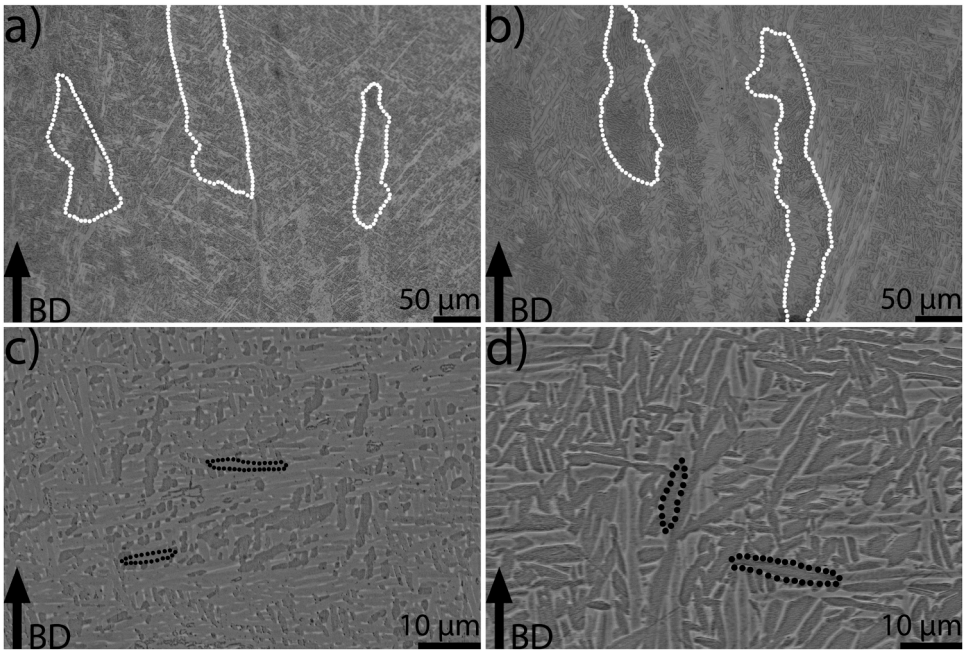

Fig. 2. Low magnification LOM images showing the prior β grain boundaries (white markings in images a & b) for modified HIP (image a) and standard HIP-treated (image b) materials. Higher magnification SEM images showing the α laths (black marking in c & d) for modified HIP (image c) and standard HIP-treated (image d) materials.

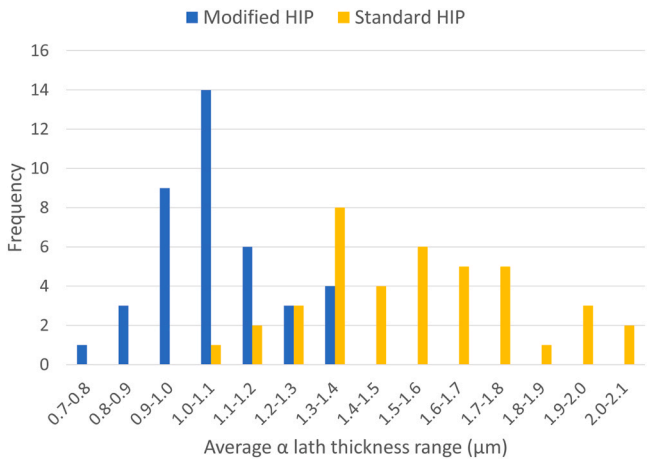

Fig. 3. Distribution of average α lath thickness measurement for modified HIP and standard HIP-treated materials.

The distribution of average α lath thickness measured parallel and perpendicular to BD for both the HIP-treated materials is presented in Fig. 3. The standard HIP-treated material had a broader spread in the measured α lath thickness and varied between 1 and 2.1 μm. The modified HIP-treated material had a comparatively small range of 0.7–1.4 μm. The consolidated average α lath thickness for the standard HIP-treated material is 1.55 ± 0.25 μm, and for the modified HIP-treated material is 1.07 ± 0.14 μm.

Fig. 4(a-c) shows the different defects seen in the material in as-built, modified HIP and standard HIP-treated conditions. The as-built material primarily had two types of defects, as seen in Fig. 4(a), gas porosity indicated by a white arrow and LoF defect indicated by a black arrow. Fig. 4(b & c) shows that the materials have some defects even after HIP treatment, but they are relatively smaller in size and lesser in number than as-built material.

The average porosity area % and relative density, measured by image analysis across the cross-section parallel to the BD for the three different types of specimens, are presented in Table 2. The density values measured by the Archimedes principles as per ASTM B311–17 for the different materials are summarized in Table 2. A nominal density of 4.43 gm/cc was used to calculate the relative density in the Archimedes method. The as-built material has a higher porosity and lower density value than the HIP-treated materials. The modified HIP-treated material has porosity levels and density values similar to the standard HIP-treated material.

3.2. Low cycle fatigue life

Fig. 5 shows the fatigue life of the modified and standard HIP-treated specimens tested at two different strain range, 0.9% and 1.2%. The number of cycles to failure is about 10^4 cycles for 1.2% strain range, and at 0.9% strain range, the fatigue life varied between about 5×10^4 to greater than one million cycles. As seen, for the 0.9% strain range, there is a large scatter in fatigue life for both HIP-treated materials. For comparison the reference data for a standard HIP-treated PBF-EB built material from S. L. Draper et al. [35] is also plotted. The reference data [35] also showed a similar spread in fatigue life at about 0.9% strain range. Three specimens were found to have failure at the threads during the test. Specimens that had thread failures are represented as solid-filled markers in the plot, and they have a life greater than one million cycles. The elastic strain-life curves derived from the Basquin relation as shown in Eq. 2 are also plotted for both HIP-treated materials. The constants for the elastic strain-life relation are obtained using the linear regression analysis described in ASTM E739–10(2015). The constants for the HIP-treated materials are listed in Table 3. As the material did not experience significant plastic strain in the tested strain range, there was insufficient data to generate the plastic strain-life curve using Eq. 3. Concerning the elastic strain-life curve, the life for standard HIP-treated material is greater by about a factor of 2 as compared to modified HIP-treated material at 0.9% strain range, but the minimum life for the HIP-treated materials did not have any significant difference. Strain-life data for as-built material tested at 1% strain range from Sandell et al. [36] is added in the plot for comparison. The as-built material [36] had about 2.5x to 4.5x lower life than the HIP-treated materials investigated in this study.

The mid-life hysteresis loops of one of the modified and one of standard HIP-treated specimens tested at 0.9% and 1.2% strain range are presented in Fig. 6. The cyclic behavior is generally elastic, with a minimal plastic strain range (about 0.02%) observed for the standard HIP-treated material at a higher strain range of 1.2%. Since there was no significant plastic strain in the material the Ramberg-Osgood relation was not utilized to generate the cyclic stress-strain curve.

The stress evolution over the number of cycles to failure for the HIP-treated specimens tested at two different strain ranges is shown in Fig. 7. At the low strain range, the specimens mostly exhibit cyclic saturation until failure. In the case of specimens tested at a high strain range, some degree of cyclic softening behavior is observed mainly for the standard HIP-treated specimen during the tensile part of the cyclic load. It is observed during the first ten cycles the stress range gradually increases, primarily due to the stabilization of the strain to match within 0.1% of the target strain range.

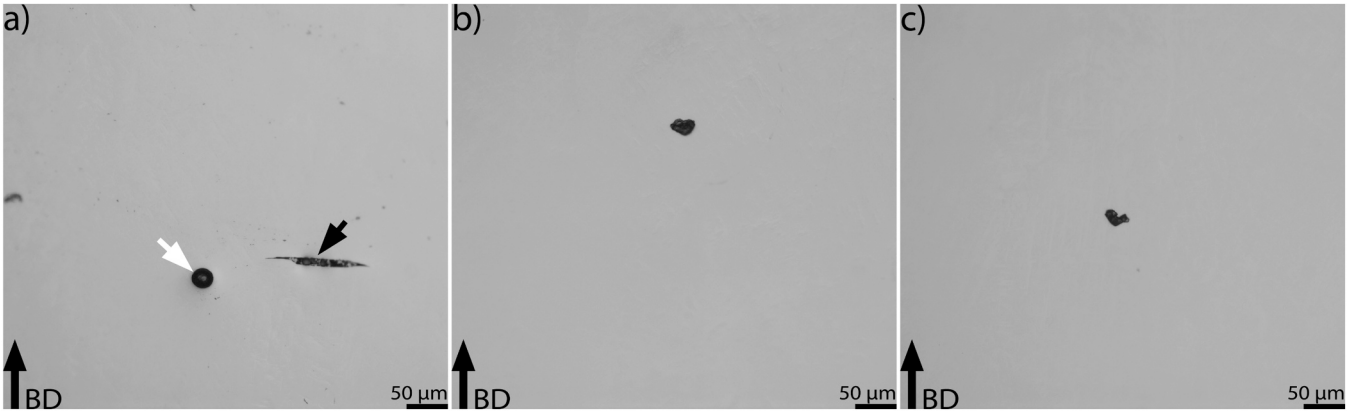

Fig. 4. Defects in the material along the BD a) As-built. The white arrow refers to gas porosity, and the small black arrow on the right side of the image points out the LoF defect b) Modified HIP-treated c) Standard HIP-treated.

Table 2
Average porosity for as-built and HIP-treated materials. Image analysis of porosity performed on images taken parallel to BD and porosity calculation by Archimedes method as per ASTM B311–17.

Specimen description	Image analysis		Archimedes principle	
	Average porosity area %	Relative density %	Measured average density (gm/cc)	Relative density %
As-built	0.2127 ± 0.0100	99.7873	4.4178 ± 0.0001	99.7256
Modified HIP	0.0063 ± 0.0034	99.9937	4.4274 ± 0.0003	99.9412
Standard HIP	0.0030 ± 0.0008	99.9970	4.4279 ± 0.0002	99.9519

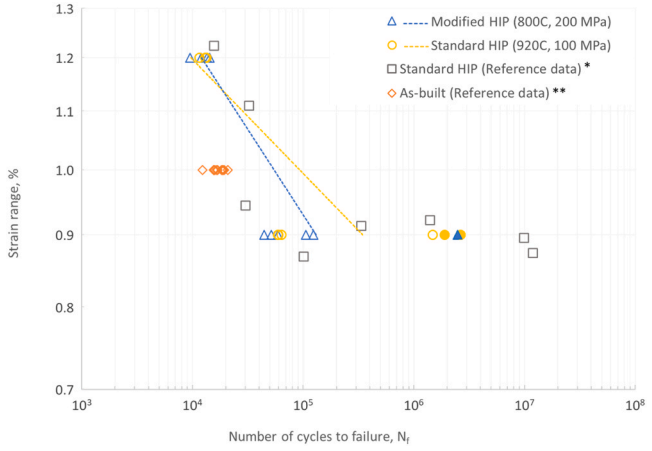

Fig. 5. Strain-life data and elastic strain-life curves for the different HIP-treated materials. Solid-filled markers represent failure at threads. The reference data of a standard HIP-treated PBF-EB material from S. L. Draper et al. [35] * and As-built material from Sandell V et al. [36] * * are added for comparison.

Table 3
Elastic strain-life relationship constants.

Material description	A	α
Modified HIP	0.04	-0.12
Standard HIP	0.03	-0.08

3.3. Fractography

The images of the fracture surfaces obtained from the LCF test are shown in Fig. 8. The low magnification stereomicroscope images on the left side in Fig. 8 show an overview of the fracture surface highlighting crack initiation location and propagation. The high magnification SEM images on the right side in Fig. 8 show the defect morphology or the smooth facet that initiated the failure. The defects are primarily non-circular in shape and are typically less than 100 μm in size. The defect sizes are presented in Table 4. Even though defects critical to fatigue life are mainly located at the machined surface, they are still in the bulk of the built material.

3.4. FCG and fatigue life prediction using NASGRO

The fatigue crack growth rate versus the ΔK curves for the standard and modified HIP-treated materials in the Paris region is shown in Fig. 9. The crack grows relatively faster in the modified HIP-treated material for values of $\Delta K < 27\ \mathrm{MPa}\sqrt{\mathrm{m}}$. In contrast, the curve for standard HIP-treated material exhibits a higher crack growth rate for $\Delta K > 27\ \mathrm{MPa}\sqrt{\mathrm{m}}$. As shown in Fig. 10, more cylces were consumed for the crack to grow in standard HIP-treated material than the modified HIP-treated material. For instance, the number of cycles required for the crack to grow from ~0.55 mm to ~1 mm was about 23000 cycles for modified HIP-treated material and about 45000 cycles for standard HIP-treated material.

An example image of the defect size measurement is shown in Fig. 11. The size definitions used for the NASGRO simulation are indicated in the image and the white markings in the image helps to visualize the shape of the defect.

A summary of the actual fatigue life and mid-life stresses from the LCF test, together with different types of crack initiation from fractography, are listed in Table 4. Five specimens (SH1, SH2, SH7, SH8 and

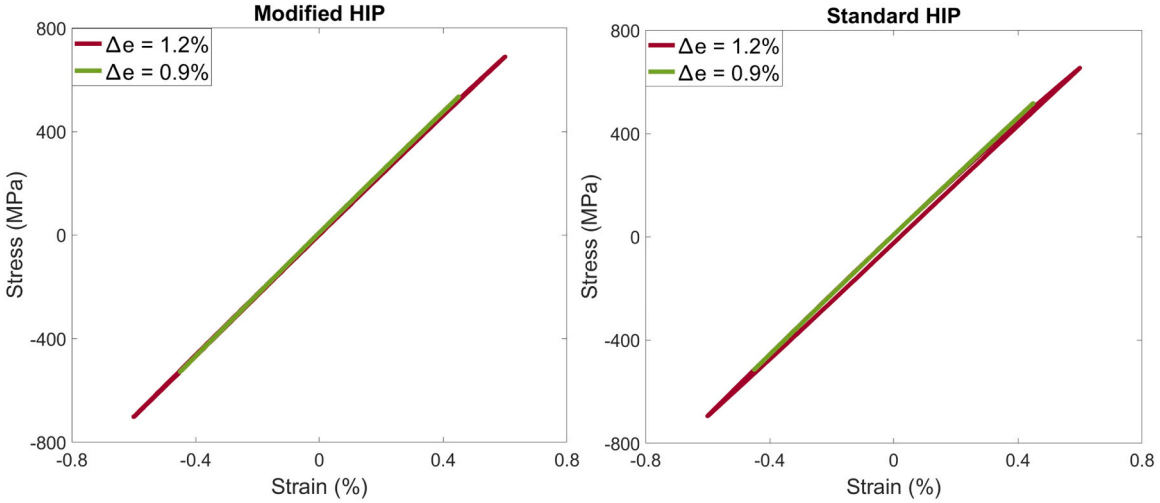

Fig. 6. Mid-life hysteresis loop at different tested strain range for the modified HIP and standard HIP-treated materials.

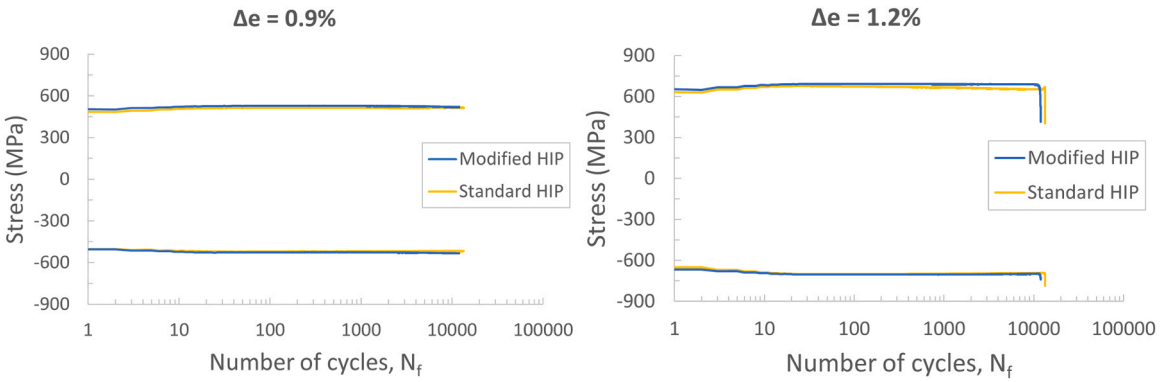

Fig. 7. Stress evolution of the standard HIP and modified HIP-treated materials at different strain ranges.

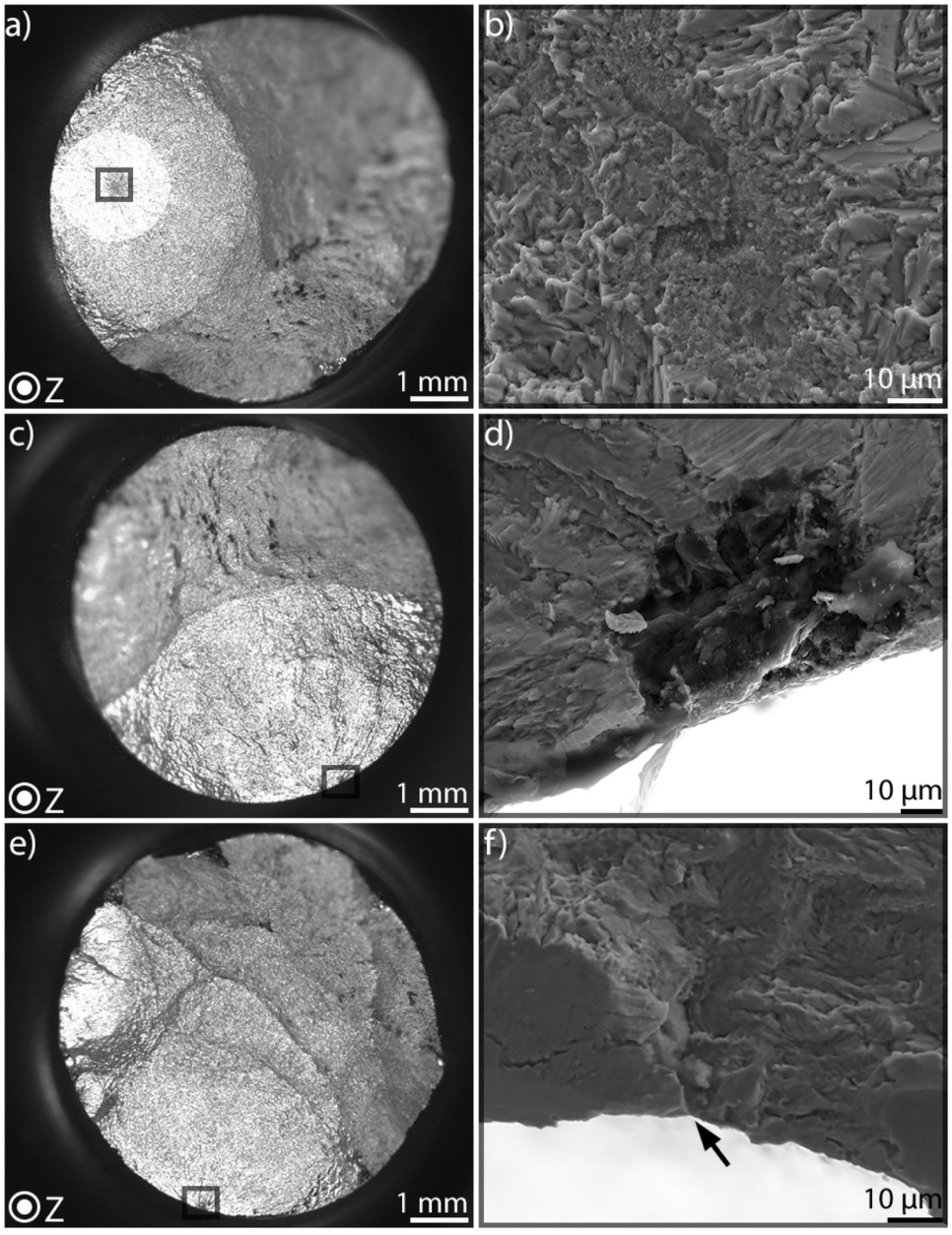

Fig. 8. Fracture surfaces showing primary crack initiation sites. Stereomicroscope images of the specimen with crack initiation site highlighted by a black square box representing failure from a) defect in bulk material, c) surface defect and e) smooth facet. Higher magnification SEM images of the crack initiation site showing b) defect in bulk material, d) surface defect and f) crack origin at a smooth facet (pointed by a black arrow).

Table 4
Summary of experimental and NASGRO predicted fatigue life. Fatigue life predictions were performed for failures from surface defects. *Crack initiation site:* $^{+}$ *- Smooth facet,* $^{++}$ *- Thread failure, * - surface defect,* ** *- defect in bulk material.*

Specimen ID	Strain range (%)	Actual cycles to failure (A)	Maximum stress (MPa)	Minimum stress (MPa)	Defect size a x 2c (μm)	Predicted cycles to failure (P)	P/A
SH1^{+}	0.9	1483539	523	-531	NA	NA	NA
SH2^{+}	0.9	63644	524	-495	NA	NA	NA
SH3^{++}	0.9	2654501	NA	NA	NA	NA	NA
SH4^{++}	0.9	1892910	NA	NA	NA	NA	NA
SH5*	0.9	59893	534	-528	47 × 48	121188	2.0
SH6*	0.9	59290	518	-515	95 × 55	87586	1.5
SH7^{+}	1.2	11552	674	-703	NA	NA	NA
SH8^{+}	1.2	13041	675	-675	NA	NA	NA
SH9*	1.2	13409	655	-694	13 × 48	86783	6.5
SH10*	1.2	13206	676	-689	44 × 84	34253	2.6
MH1^{++}	0.9	2487245	NA	NA	NA	NA	NA
MH2**	0.9	123146	535	-528	32 × 39	NA	NA
MH3*	0.9	58912	501	-614	23 × 42	84564	1.4
MH4*	0.9	105703	435	-641	21 × 59	87016	0.8
MH5*	0.9	44345	533	-514	33.5 × 63	78777	1.8
MH6*	0.9	51635	517	-536	44 × 73	66344	1.3
MH7^{+}	1.2	13518	691	-752	NA	NA	NA
MH8**	1.2	14347	659	-758	25 × 32	NA	NA
MH9*	1.2	9534	666	-779	16.5 × 29	44822	4.7
MH10*	1.2	11998	689	-701	54 × 78	22956	1.9

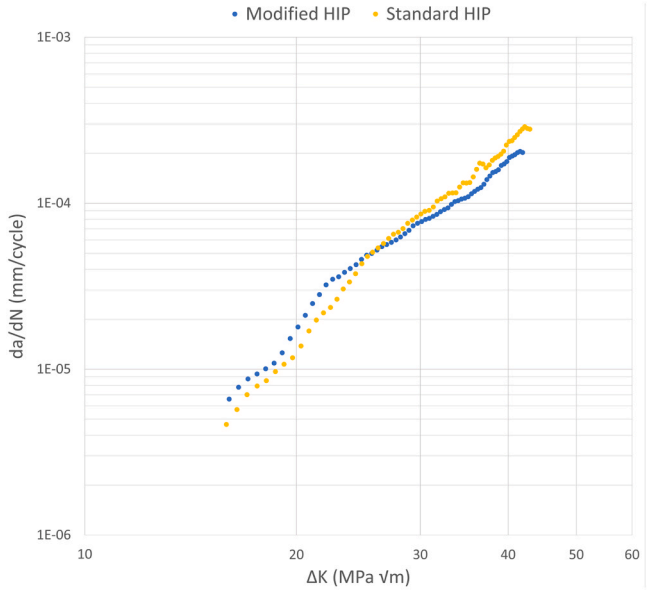

Fig. 9. Crack growth versus ΔK in the Paris region for modified HIP and standard HIP-treated materials.

MH7) had fractures originating from the smooth facet, while three specimens (SH3, SH4 and MH1) had failures at the thread. Among the specimens that had fractures initiating from a defect, two specimens (MH2 and MH8) had a defect in the bulk material, and the remaining specimens had a surface defect. The predicted fatigue life using NASGRO for specimens where the crack initiated from the surface defect is shown in Table 4. The ratio of predicted to experimental fatigue life is also shown in Table 4, which helps to evaluate the linear elastic fracture mechanics (LEFM) tool's capability for life predictions. In most cases, the ratio was about 1–2, indicating the predicted life is comparable to the experimental values. There were few outliers with ratios around 5–6.5, particularly for very small defects.

4. Discussion

4.1. Effect of microstructure and porosity on fatigue properties

The β → α phase transformation in PBF-EB built Ti-6Al-4 V takes place following a specific Burgers orientation relationship, where depending on the cooling rate, a single β grain can transform into 12 α variants with different orientations. The α laths are first formed along the β grain boundary termed as grain boundary α (GB-α). As the transformation continues, α laths start to nucleate from the β grain boundary or GB-α, as well as from the boundary of previously formed α laths. So, PBF-EB built Ti-6Al-4 V significantly have an intertwined basketweave microstructure [26] same has been observed in the current study, resulting in randomly oriented α laths. Galarraga et al. [37] found that when the post-heat treatment is performed below the β transus temperature down to 600 C, coarsening of α laths occurs as a function of temperature and time. A similar effect was observed in the current study, with the standard HIP being performed at a higher temperature than the modified HIP resulted in relatively coarser α laths.

When such PBF-EB built HIP-treated material is subjected to cyclic loading, the failure is highly localized and driven by specific deformation mechanisms such as slip or twinning. The modified HIP-treated material has a finer basketweave microstructure with a comparatively smaller dislocation slip length than standard HIP-treated material. The microstructural feature that increases the yield strength and/or reduces the slip length resists crack initiation and helps to improve the fatigue strength of the material [38]. As the crack propagates, the crack front geometry deviates from the average propagation plane in a direction determined by the slip planes in the adjacent areas and a distance defined by the microstructural feature size [26]. So the degree of resistance to crack propagation is influenced by the microstructural feature size. In the present study, the crack propagation has been observed to be dominant in defining the fatigue life as the standard HIP-treated material with a coarser microstructure has a higher fatigue life as shown in Fig. 5.

Oh et al. [39] has reported that crack initiation mainly occurred at prior β grain boundary in electron beam welded investment castings. Åkerfeldt et al. observed crack initiation to occur close to prior β grain boundaries in laser metal wire deposited Ti-6Al-4 V, but for specimens tested parallel to deposition direction, not in specimens tested perpendicular to deposition direction [40]. In the present study, the samples

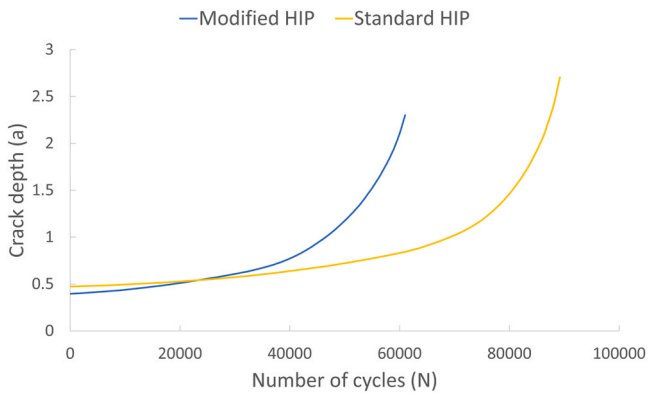

Fig. 10. Crack length versus number of cycles plot for modified HIP and standard HIP-treated material from the FCG test.

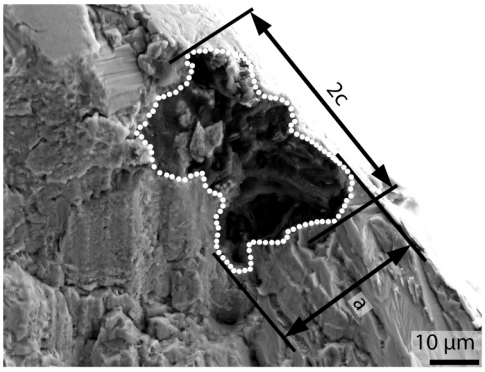

Fig. 11. Image showing defect size measurement description used as an input for fatigue life predictions in NASGRO. The white marking helps to visualize the defect morphology.

were tested parallel to the build direction. The microstructural induced failures are most likely to occur in the α laths resulting in smooth facets at the failure site. In the current study, for five specimens the crack initiated from a smooth facet similar to that found in a defect-free conventional Ti-6Al-4 V material [25]. Smooth facets are formed in lamellar colonies that have their basal plane oriented perpendicular to the loading direction and their adjacent colonies oriented favourably for slip to occur [25]. The prior β grain may also affect the fatigue properties indirectly by influencing the orientation of the α phase and the size of the α colonies as they grow from these grain boundaries. The GB α laths formed along the prior β grain boundaries have been reported to affect the elongation property but not the LCF of AM-built Ti-6Al-4 V [40].

In general, the fatigue failures in PBF-EB built HIP-treated Ti-6Al-4 V machined specimens are dependent not only on microstructure but also on internal defects. The effect of HIP treatment on eliminating the internal pores and improving the bulk fatigue performance of PBF-EB built Ti-6Al-4 V has been well established [26,29]. The quantitative result in Table 2 shows that the HIP treatment produces nearly fully dense material. Also, there was no significant difference in the relative density of the modified and standard HIP-treated material, indicating the modified HIP treatment effectively eliminates the pores. Investigation of the fracture surface in this study showed that 60% of the tested specimens failed from a non-spherical defect (LoF defect) that are less than 100 µm in size. So, this indicates that there could be fatigue-critical size LoF defects in the material even after HIP treatment.

4.2. Strain-life

The strain-life data in Fig. 5 shows a scatter in fatigue life for both the HIP-treated materials, particularly for specimens tested at 0.9% strain range. It is common to have scatter in the low cycle fatigue life at a specific strain range due to variability in the quality of specimen and testing condition [41]. The high cycle fatigue data from the literature [35] also showed there is scatter in the fatigue life around the 0.9% strain range. As the strain-controlled test is performed at $R = -1$, it is possible to compare the life data from the stress-controlled test as there is negligible plastic deformation observed at this strain range. Plaskitt et al.[42] reported similar results where HIP treated samples had less scatter in fatigue life at high strain amplitude (low life) and more scatter at low strain amplitude (long life). Also, the improvement in in fatigue life due to HIP treatment was noted only for the samples tested at low strain amplitude. The cycles to failure in standard HIP-treated material ranged from around 60 000 cycles to one million cycles, whereas in modified HIP-treated material, the life was between about 45 000–125 000 cycles at 0.9% strain range. If the specimens failed at threads were also considered, the fatigue life scatter range further increases. However, the difference in the lowest life to failure for both the HIP-treated materials is insignificant. Based on this limited test data, it appears the modified HIP-treated material has a similar fatigue performance to standard HIP-treated material.

In general, cyclic softening or hardening occurs in the metallic alloys subjected to fatigue loading [41]. As seen in Fig. 7, the specimens tested at strain ranges that resulted in primarily elastic cyclic response displayed no significant softening or hardening behavior until failure. Some degree of cyclic softening was observed for the standard HIP-treated material in the tensile regime of the cyclic load that for specimens that exhibited some plastic cyclic response. It can be found in the literature that the softening or hardening behavior is related to the microstructure and mechanical properties of the material [43]. The standard HIP-treated material with coarser microstructure is reported to have a lower yield strength than the modified HIP-treated material [31,44]. Consequently, the softening behavior seen in the standard HIP-treated material at high strain ranges could be related to its low yield strength property.

The mid-life hysteresis loops in Fig. 6 show that the stress response at the low strain range is primarily elastic, and some degree of cyclic plasticity is observed for the high strain range in the standard HIP-treated specimen. Again the lower yield strength property of the standard HIP-treated specimen could have resulted in yielding when subjected to a high strain range.

4.3. FCG and NASGRO fatigue life predictions

In PBF-EB manufactured material the microstructure is primarily basketweave with limited quantity of α colonies [26,45,46], similar observations are made in the current study. The mechanism governing the crack propagation in such a microstructure involves two adjacent α laths with different orientations, causing the crack front to deviate locally and propagate in a direction based on the slip planes in these adjacent α laths [26]. The crack front is bifurcated and forced to travel in an unfavorable direction and orientation over a distance defined by the microstructural feature size, the α lath thickness. Therefore, the coarser α laths in standard HIP-treated material would potentially offer higher resistance to crack propagation as compared to the modified HIP-treated material that has relatively finer α laths. This behavior is evident in the crack propagation plots shown in Fig. 9 and Fig. 10, where a slower growth rate is observed for the standard HIP-treated material. But, compared to the scatter in the fatigue life observed at low strain range in Fig. 5 and the number of FCG samples tested, the difference in crack propagation rate between different HIP-treated materials is considered statistically insignificant.

Table 4 indicates that fracture mostly initiated from defects in standard and modified HIP-treated materials. It shows that the HIP treatments effectively closed most of the circular gas pores, and the small irregular LoF defects that are still present served as the crack initiation sites. The crack initiating defects were located at the surface for most failed specimens. It has been found in the literature that near-surface pores are more detrimental to fatigue life [14]. The main reason is that the defects closer to the surface generates higher or larger stress intensity factor compared to internal defects of same size as suggested by Murakami [47]. Consequently, the "semi-elliptical surface crack in plate" case (SC30) in NASGRO, was preferred for life prediction. As reported in Table 4, the NASGRO predicted lives are mainly within a factor of 1–2 when compared to measured lives. In cases with extremely small defect size the predicted life was about 4–6 times higher than the measured life. This overprediction of life by NASGRO could be attributed to the behavior of short cracks in the near-threshold region. In this study, the NASGRO life predictions were carried out using crack growth test data produced in the Paris region, where the minimum crack size was about 300–500 μm and the corresponding ΔK value was about 15–16 MPa$\sqrt{m}$. Extrapolating the crack growth curve to a near threshold region, where $\Delta K < \Delta K_{th}$ of long crack could lead to less accurate life predictions. It can be found in literature that the short cracks have higher crack growth rate than corresponding large cracks for the same ΔK and it may not be appropriate to employ LEFM to predict fatigue life for such scenarios [48]. The smallest intrinsic crack length (a_o) below which the LEFM based approach using long crack data will be nonconservative is determined by Eq. 5 [48].

$$a_o = 1/\pi + (\Delta K_{th}/\Delta\sigma_e)^2 \quad (5)$$

Where ΔK_{th} is threshold SIF range and $\Delta\sigma_e$ is the fatigue limit stress range. In the case of conventional Ti6-Al-4 V, with ΔKth of 6 MPa$\sqrt{m}$ [48] and $\Delta\sigma_e$ of 750 MPa [48], the intrinsic crack size is about 20 μm. The intrinsic crack size is empirical in nature [48] and needs to be established for the investigated materials. Also, in the case of short cracks, the crack propagation rate increases with an increase in σ_{max} [49]. A combined effect of very small defect size and higher σ_{max} (for 1.2% strain range) have resulted in overprediction of fatigue life using NASGRO in the current study.

5. Conclusions

In this study, the fatigue performance of standard HIP and low-temperature HIP-treated PBF-EB built materials were investigated and resulted in the following conclusions.

- Modified HIP-treated material with finer microstructure exhibited comparable fatigue life to the coarser standard HIP-treated material.
- At low strain range, a large scatter in fatigue life was observed for both of the HIP-treated materials.
- At 0.9% strain range, the elastic strain-life curves indicated a 2x higher fatigue life for the standard HIP-treated material compared to the modified HIP-treated material, however, the difference in minimum life is less prominent.
- The HIP-treated materials experienced fully elastic cyclic behavior at 0.9% strain range, and at 1.2% strain range, limited plasticity was observed in the material with lower yield strength.
- Cyclic softening was observed in standard HIP-treated material at a higher strain range due to coarsening of α laths and reduced yield strength from the HIP treatment.
- NASGRO is less accurate in predicting the fatigue life of material with a defect smaller than intrinsic crack length (a_o) due to the limitation of LEFM in predicting short fatigue crack propagation.

CRediT authorship contribution statement

Karthikeyan Thalavai Pandian: Methodology, Investigation, Validation, Formal analysis, Writing – original draft preparation. **Magnus Neikter:** Supervision, Writing – reviewing and editing. **Fouzi Bahbou:** Conceptualization, Resources, Writing – reviewing and editing. **Ashish Ganvir:** Project administration, Funding acquisition, Writing – reviewing and editing. **Thomas Hansson:** Conceptualization, Supervision, Writing – reviewing and editing. **Robert Pederson:** Supervision, Funding acquisition, Project administration.

Declaration of Competing Interest

The authors declare the following financial interests/personal relationships which may be considered as potential competing interests: Karthikeyan Thalavai Pandian reports financial support was provided by Sweden's Innovation Agency. Karthikeyan Thalavai Pandian reports a relationship with Sweden's Innovation Agency that includes: funding grants.

Data availability

The raw/processed data required to reproduce these findings cannot be shared at this time as the data also forms part of an ongoing study.

Acknowledgment

The authors want to acknowledge the support from GE-Additive, Sweden in providing the PBF-EB built material for this research. The help from Quintus Technologies AB for HIP-treatment of the test specimens is much appreciated. The authors are grateful to Mats Högström at University West for performing the LCF tests. Finally, the authors would like to thank GKN Aerospace Sweden AB and AIM Sweden AB for its continuous support. Financial support from VINNOVA, through the "Nationella flygtekniska forskningsprogrammet 7" (NFFP) (project #: 2019–02741), is highly appreciated.

References

[1] R.R. Boyer, An overview on the use of titanium in the aerospace industry, Mater. Sci. Eng.: A 213 (1996) 103–114, https://doi.org/10.1016/0921-5093(96)10233-1.
[2] G. Lütjering, J.C. Williams, Titanium, 2nd ed., Springer, Berlin Heidelberg, 2007.
[3] R. Dehoff, C. Duty, W. Peter, Y. Yamamoto, W. Chen, C. Blue, C. Tallman, Case study: Additive manufacturing of aerospace brackets, Advanced Materials and Processes. 171 (2013) 19–22. ⟨http://www.ornl.gov/sci/manufacturing/video/⟩ (accessed November 15, 2021).
[4] S. Rawal, J. Brantley, N. Karabudak, Additive manufacturing of Ti-6Al-4 V alloy components for spacecraft applications, RAST 2013 - Proceedings of 6th International Conference on Recent Advances in Space Technologies. (2013) 5–11. https://doi.org/10.1109/RAST.2013.6581260.
[5] H.P. Tang, Q.B. Wang, G.Y. Yang, J. Gu, N. Liu, L. Jia, M. Qian, A Honeycomb-Structured Ti-6Al-4 V Oil–Gas Separation rotor additively manufactured by selective electron beam melting for aero-engine applications, JOM 68 (2016) 799–805, https://doi.org/10.1007/S11837-015-1778-9/TABLES/4.
[6] A. Gisario, M. Kazarian, F. Martina, M. Mehrpouya, Metal additive manufacturing in the commercial aviation industry: a review, J. Manuf. Syst. 53 (2019) 124–149, https://doi.org/10.1016/J.JMSY.2019.08.005.
[7] S. Singamneni, Y. Lv, A. Hewitt, R. Chalk, W. Thomas, D. Jordison, Additive manufacturing for the aircraft industry: a review, J. Aeronaut. Aerosp. Eng. 8 (2019) 215, https://doi.org/10.35248/2168-9792.19.8.215.
[8] M. Neikter, Microstructure and hydrogen embrittlement of additively manufactured Ti-6Al-4 V, PhD Thesis, Luleå University of Technology, Luleå,. (2019).
[9] S.S. Al-Bermani, M.L. Blackmore, W. Zhang, I. Todd, The origin of microstructural diversity, texture, and mechanical properties in electron beam melted Ti-6Al-4 V, Met. Mater. Trans. A Phys. Met. Mater. Sci. 41 (2010) 3422–3434, https://doi.org/10.1007/S11661-010-0397-X.
[10] S. Rawal, J. Brantley, N. Karabudak, Additive manufacturing of Ti-6Al-4 V alloy components for spacecraft applications, RAST 2013 - Proceedings of 6th International Conference on Recent Advances in Space Technologies. (2013) 5–11. https://doi.org/10.1109/RAST.2013.6581260.
[11] L.E. Murr, E. v Esquivel, S.A. Quinones, S.M. Gaytan, M.I. Lopez, E.Y. Martinez, F. Medina, D.H. Hernandez, E. Martinez, J.L. Martinez, S.W. Stafford, D.K. Brown,

T. Hoppe, W. Meyers, U. Lindhe, R.B. Wicker, Microstructures and mechanical properties of electron beam-rapid manufactured Ti–6Al–4 V biomedical prototypes compared to wrought Ti–6Al–4 V, Mater. Charact. 60 (2009) 96–105, https://doi.org/10.1016/J.MATCHAR.2008.07.006.

[12] M. Koike, P. Greer, K. Owen, G. Lilly, L.E. Murr, S.M. Gaytan, E. Martinez, T. Okabe, Evaluation of titanium alloys fabricated using rapid prototyping technologies—electron beam melting and laser beam melting, Pages 1776-1792, Materials 2011 Vol. 4 (4) (2011) 1776–1792, https://doi.org/10.3390/MA4101776.

[13] P. Edwards, A. O'Conner, M. Ramulu, Electron beam additive manufacturing of titanium components: Properties and performance, Journal of Manufacturing Science and Engineering, Trans. ASME 135 (2013), https://doi.org/10.1115/1.4025773/375746.

[14] S. Tammas-Williams, P.J. Withers, I. Todd, P.B. Prangnell, The Influence of Porosity on Fatigue Crack Initiation in Additively Manufactured Titanium Components, Sci. Rep. 7 (2017) 1–13, https://doi.org/10.1038/s41598-017-06504-5.

[15] P. Li, D.H. Warner, A. Fatemi, N. Phan, Critical assessment of the fatigue performance of additively manufactured Ti-6Al-4 V and perspective for future research, Int J. Fatigue (2016), https://doi.org/10.1016/j.ijfatigue.2015.12.003.

[16] L. Ladani, M. Sadeghilaridjani, Review of powder bed fusion additive manufacturing for metals, Page 1391, Metals 2021 Vol. 11 (11) (2021) 1391, https://doi.org/10.3390/MET11091391.

[17] L. Facchini, E. Magalini, P. Robotti, A. Molinari, Microstructure and mechanical properties of Ti-6Al-4V produced by electron beam melting of pre-alloyed powders, Rapid Prototyp. J. 15 (2009) 171–178, https://doi.org/10.1108/13552540910960262.

[18] M. Neikter, M. Colliander, C. de, A. Schwerz, T. Hansson, P. Åkerfeldt, R. Pederson, M.-L. Antti, Fatigue crack growth of electron beam melted Ti-6Al-4 V in high-pressure hydrogen, Materials 13 (2020) 1287, https://doi.org/10.3390/MA13061287.

[19] J. Bruno, A. Rochman, G. Cassar, Effect of build orientation of electron beam melting on microstructure and mechanical properties of Ti-6Al-4 V, J. Mater. Eng. Perform. 26 (2017) 692–703, https://doi.org/10.1007/S11665-017-2502-4.

[20] S. Ghods, E. Schultz, C. Wisdom, R. Schur, R. Pahuja, A. Montelione, D. Arola, M. Ramulu, Electron beam additive manufacturing of Ti6Al4V: Evolution of powder morphology and part microstructure with powder reuse, Mater. (Oxf.) 9 (2020), 100631, https://doi.org/10.1016/J.MTLA.2020.100631.

[21] S.D. Henry, K.S. Dragolich, N.D. DiMatteo, A.S.M. International, Fatigue Data Book: Light Structural Alloys, ASM International, 1994.

[22] G.T. Gray, A.W. Thompson, J.C. Williams, Influence of microstructure on fatigue crack initiation in fully pearlitic steels, 16:5, Metall. Trans. A 1985 16 (1985) 753–760, https://doi.org/10.1007/BF02814826.

[23] G. Lütjering, Influence of processing on microstructure and mechanical properties of (α+β) titanium alloys, Mater. Sci. Eng.: A 243 (1998) 32–45, https://doi.org/10.1016/S0921-5093(97)00778-8.

[24] B. Baufeld, O. van der Biest, Mechanical properties of Ti-6Al-4 V specimens produced by shaped metal deposition, Sci. Technol. Adv. Mater. 10 (2009) 15008–15018, https://doi.org/10.1088/1468-6996/10/1/015008.

[25] R.K. Nalla, B.L. Boyce, J.P. Campbell, J.O. Peters, R.O. Ritchie, Influence of microstructure on high-cycle fatigue of Ti-6Al-4 V: bimodal vs. lamellar structures, 33:3, Metall. Mater. Trans. A 2002 33 (2002) 899–918, https://doi.org/10.1007/S11661-002-0160-Z.

[26] H. Galarraga, R.J. Warren, D.A. Lados, R.R. Dehoff, M.M. Kirka, Fatigue crack growth mechanisms at the microstructure scale in as-fabricated and heat treated Ti-6Al-4 V ELI manufactured by electron beam melting (EBM, Eng. Fract. Mech. 176 (2017) 263–280, https://doi.org/10.1016/J.ENGFRACMECH.2017.03.024.

[27] S. Tammas-Williams, H. Zhao, F. Léonard, F. Derguti, I. Todd, P.B. Prangnell, XCT analysis of the influence of melt strategies on defect population in Ti–6Al–4 V components manufactured by selective electron beam melting, Mater. Charact. 102 (2015) 47–61, https://doi.org/10.1016/J.MATCHAR.2015.02.008.

[28] R. Cunningham, A. Nicolas, J. Madsen, E. Fodran, E. Anagnostou, M.D. Sangid, A. D. Rollett, Analyzing the effects of powder and post-processing on porosity and properties of electron beam melted Ti-6Al-4 V, Mater. Res. Lett. 5 (2017) 516–525, https://doi.org/10.1080/21663831.2017.1340911.

[29] D. Greitemeier, F. Palm, F. Syassen, T. Melz, Fatigue performance of additive manufactured TiAl6V4 using electron and laser beam melting, Int J. Fatigue 94 (2017) 211–217, https://doi.org/10.1016/j.ijfatigue.2016.05.001.

[30] A. Mohammadhosseini, D. Fraser, S.H. Masood, M. Jahedi, Microstructure and mechanical properties of Ti–6Al–4 V manufactured by electron beam melting process, Mater. Res. Innov. 17 (2013) s106–s112, https://doi.org/10.1179/1432891713Z.000000000302.

[31] A. Eklund, M. Ahlfors, F. Bahbou, J. Wedenstrand, Optimizing HIP and printing parameters for EBM Ti-6Al-4 V, Key Eng. Mater., Trans. Tech. Publ. Ltd (2018) 174–178, https://doi.org/10.4028/www.scientific.net/KEM.770.174.

[32] Wayne Rasband, ImageJ., National Institutes of Health, USA. (n.d.). https://imagej.nih.gov/ij.

[33] N. Ridley, REVIEW OF THE DATA ON THE INTERLAMELLAR SPACING OF PEARLITE., in: Metallurgical Transactions. A, Physical Metallurgy and Materials Science, 1983: pp. 1019–1036. https://doi.org/10.1007/bf02644694.

[34] NASGRO® Fracture Mechanics & Fatigue Crack Growth Software | SwRI, (n.d.). https://www.swri.org/consortia/nasgro (accessed March 10, 2022).

[35] S.L. Draper, B.A. Lerch, J. Telesman, R.E. Martin, I.E. Locci, A. Garg, A.J. Ring, B.A. Lerch, J. Telesman, R.E. Martin, I.E. Locci, A. Garg, A.J. Ring, Materials Characterization of Electron Beam Melted Ti-6Al-4 V, (2016). http://www.sti.nasa.gov (accessed December 14, 2021).

[36] V. Sandell, T. Hansson, S. Roychowdhury, T. Månsson, M. Delin, P. Åkerfeldt, M. L. Antti, Defects in Electron Beam Melted Ti-6Al-4 V: Fatigue Life Prediction Using Experimental Data and Extreme Value Statistics, Page 640. 14, Materials 2021 Vol. 14 (2021) 640, https://doi.org/10.3390/MA14030640.

[37] H. Galarraga, R.J. Warren, D.A. Lados, R.R. Dehoff, M.M. Kirka, P. Nandwana, Effects of heat treatments on microstructure and properties of Ti-6Al-4 V ELI alloy fabricated by electron beam melting (EBM, Mater. Sci. Eng.: A 685 (2017) 417–428, https://doi.org/10.1016/J.MSEA.2017.01.019.

[38] G. Lütjering, A. Gysler, Critical Review-Fatigue, in: Titanium Science and Technology, Proceedings of Fifth International Conference on Titanium, 1984: p. 2071.

[39] J. Oh, N.J. Kim, S. Lee, E.W. Lee, Correlation of fatigue properties and microstructure in investment cast Ti-6Al-4 V welds, Mater. Sci. Eng. A 340 (2003) 232–242, https://doi.org/10.1016/S0921-5093(02)00176-4.

[40] P. Åkerfeldt, R. Pederson, M.L. Antti, A fractographic study exploring the relationship between the low cycle fatigue and metallurgical properties of laser metal wire deposited Ti–6Al–4 V, Int J. Fatigue 87 (2016) 245–256, https://doi.org/10.1016/J.IJFATIGUE.2016.02.011.

[41] S. Suresh, Fatigue of Materials, Cambridge University Press, 1998, https://doi.org/10.1017/CBO9780511806575.

[42] R. Plaskitt, A. Halfpenny, M. Hill, Strain controlled fatigue testing of additive manufactured titanium alloy Ti-6Al-4 V, Lecture Notes in, Mech. Eng. (2020) 43–55, https://doi.org/10.1007/978-3-030-21503-3_4/COVER.

[43] Z. Zhang, Cyclic Hardening/Softening, in: Q.J. Wang, Y.-W. Chung (Eds.), Encyclopedia of Tribology, Springer, US, Boston, MA, 2013, pp. 687–691, https://doi.org/10.1007/978-0-387-92897-5_245.

[44] K.T. Pandian, M. Neikter, F. Bahbou, T. Hansson, R. Pederson, Elevated-Temperature Tensile Properties of Low-Temperature HIP-Treated EBM-Built Ti-6Al-4 V, Page 3624, Materials 2022 Vol. 15 (15) (2022) 3624, https://doi.org/10.3390/MA15103624.

[45] C. de Formanoir, S. Michotte, O. Rigo, L. Germain, S. Godet, Electron beam melted Ti–6Al–4 V: Microstructure, texture and mechanical behavior of the as-built and heat-treated material, Mater. Sci. Eng.: A 652 (2016) 105–119, https://doi.org/10.1016/j.msea.2015.11.052.

[46] A. Safdar, L.Y. Wei, A. Snis, Z. Lai, Evaluation of microstructural development in electron beam melted Ti-6Al-4 V, Mater. Charact. 65 (2012) 8–15, https://doi.org/10.1016/J.MATCHAR.2011.12.008.

[47] Y. Murakami, Material defects as the basis of fatigue design, Int. J. Fatigue 41 (2012) 2–10, https://doi.org/10.1016/J.IJFATIGUE.2011.12.001.

[48] S. Suresh, R.O. Ritchie, Propagation of short fatigue cracks, Int. Met. Rev. 29 (1984) 445–475, https://doi.org/10.1179/imtr.1984.29.1.445.

[49] J.A. Hines, G. Lütjering, Propagation of microcracks at stress amplitudes below the conventional fatigue limit in Ti–6Al–4 V, Fatigue Fract. Eng. Mater. Struct. 22 (1999) 657–665, https://doi.org/10.1046/J.1460-2695.1999.T01-1-00217.X.